Materials Advances

ROYAL SOCIETY OF CHEMISTRY

PAPER

View Article Online
View Journal | View Issue

Cite this: *Mater. Adv.*, 2025, 6, 9829

A conductive poly(*m*-aminophenol) interface for α-lipoic acid detection in NELL-1 membranous nephropathy

Kanwal Bashir, Adnan Mujahid and Adeel Afzal *

Conductive polymers are crucial for improving the performance of electrochemical sensors due to their tunable electronic properties and functional versatility. Poly(*m*-aminophenol) (PmAP), a conductive polymer, serves as an electroactive interface for the development of a disposable point-of-care (POC) electrochemical sensor for α-lipoic acid (LA) detection, a potential etiological trigger of neural epidermal growth factor-like 1 protein-associated membranous nephropathy (NELL-1 MN). Synthesized *via* oxidative polymerization of diphenylamine-cross-linked *m*-aminophenol, PmAP exhibits a hierarchically porous morphology and intrinsic redox activity, enabling efficient electron transfer. Immobilization onto screen-printed gold electrodes (Au-SPEs) provides a cost-effective and scalable sensing platform. Electrochemical impedance spectroscopy (EIS) reveals that PmAP significantly reduces charge-transfer resistance and enhances electron transfer kinetics. Differential pulse voltammetry (DPV) confirms that LA selectively interacts with PmAP, leading to a concentration-dependent attenuation of oxidation peak current across a 1–300 μM range. The PmAP/Au-SPE sensor achieves a sensitivity of 4.77 μA cm^{-2} μM^{-1} and a detection limit of 430 nM, demonstrating high selectivity with minimal interference from biologically relevant analytes. Additionally, the sensor achieves a recovery rate of 101% ± 6.32% in human serum, validating its clinical applicability. The integration of PmAP as a versatile polymeric interface offers a highly robust, stable, and selective platform for real-time renal function assessment and early-stage NELL-1 MN monitoring.

Received 16th May 2025,
Accepted 30th October 2025

DOI: 10.1039/d5ma00501a

rsc.li/materials-advances

Introduction

Neural epidermal growth factor-like 1 protein-associated membranous nephropathy (NELL-1 MN) is the second most prevalent antigen among patients with primary membranous nephropathy.[1] Patients with NELL-1 MN typically present with nephrotic syndrome, characterized by heavy proteinuria, hypoalbuminemia, and edema, leading to chronic kidney disease or kidney failure if not treated effectively.[2,3] NELL-1 MN has been found in the context of several diseases, including sarcoidosis, *de novo* MN in a kidney transplant, autoimmune disease, hematopoietic stem cell transplant, infections, and NELL-1 associated with malignancy.[3] In adults, the annual prevalence of NELL-1-associated membranous nephropathy is estimated at roughly 10–12 cases per million in North America and 2–17 cases per million in Europe.[4] Due to the increasing global impact of NELL-1 MN and its potential for acute complications like renal vein thrombosis as well as its association with malignancies, it increases the burden on healthcare systems.[5] It is essential to develop an economical and portable point-of-care (POC) testing method for routine monitoring.

Recent studies suggest that α-lipoic acid (LA) supplementation may trigger the onset of NELL-1 MN, making it a potent cause of this condition.[6] Although its specificity against other conditions associated with NELL-1 MN requires further large-scale validation, emerging evidence suggests that NELL-1 MN is characterized by increased LA concentration in body fluids like serum and saliva, making LA a promising candidate for monitoring NELL-1 MN.[6,7] Nonetheless, the most common traditional methods for LA determination involve the spectrophotometric detection of LA with reagents like palladium(II) chloride, resulting in a measurable change in color due to the formation of an LA complex with palladium(II) chloride.[8] However, the efficiency of the spectrophotometric method can suffer from various factors such as interference by the other compounds present in the sample, low sensitivity compared to other advanced techniques, and the need for extensive sample preparation.[9] This leads to the development of new substitutes based on high-performance liquid chromatography (HPLC),[10] gas chromatography (GC),[11] and electrochemical methods.[12]

Sensors and Diagnostics Lab, School of Chemistry, University of the Punjab, Quaid-i-Azam Campus, Lahore, 54590, Pakistan. E-mail: adeel.chem@pu.edu.pk

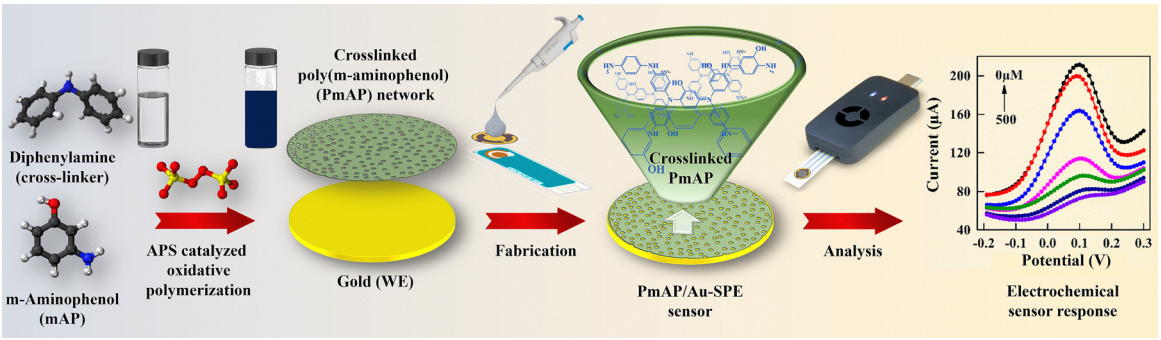

Fig. 1 A schematic representation of the synthesis of poly(*m*-aminophenol) (P*m*AP) and the fabrication of disposable P*m*AP/Au-SPE sensors for portable, wireless electrochemical detection of LA.

Unlike the traditional analytical techniques, electrochemical sensors stand out as perfect substitutes due to their advantages such as high sensitivity and selectivity, simplicity, portability, cost-effectiveness, robustness, ease of operation, and faster response.[13–15] For instance, Marin *et al.*[16] developed a selective electrochemical sensor to determine LA in human serum using a platinum electrode in an acetate buffer solution with a 13.15 μM detection limit and high sensitivity. Gungor *et al.*[17] reported an electrochemical chitosan-based polyurethane membrane-modified biosensor for practical, sensitive, and fast measurement of LA. The sensor exhibited high sensitivity with a detection limit of 4.93 μM and a wide linear detection range of 5–200 μM. Duran *et al.*[18] designed an electrochemical sensor based on a polyvanillin-modified platinum electrode to detect LA in the Britton–Robinson buffer solution and reported a detection limit of 25 μM. Recently, Karabozhikova and Tsakova[19] developed a poly(3,4-ethylenedioxythiophene) (PEDOT) based electrochemical sensor for the detection of LA that demonstrated a 6 μM detection limit and linear response in the 8–200 μM LA concentration range.

Despite recent advancements, point-of-care (POC) diagnostic technologies continue to encounter difficulties related to sensitivity, selectivity, and stability, which impede their widespread commercial adoption. Consequently, there is a pressing need to create a cost-effective and practical point-of-care device that can accurately measure LA concentration in physiological fluids. This represents a considerable challenge, given the requirements for precision, reliability, and affordability in such devices. In this study, we present the development of a selective and cost-effective non-enzymatic electrochemical sensor utilizing a conductive interface based on diphenylamine-cross-linked poly(*m*-aminophenol) (PmAP) for the detection of LA in human serum. Conductive polymers, such as PmAP and polyaniline (PAni), facilitate rapid electron transfer and provide numerous active sites for interactions with target molecules, resulting in improved detection limit and response time.[20–22]

While more conductive polymers like polyaniline exist,[23–25] PmAP is specifically selected as the electroactive sensing interface in this work because its unique structural features provide both electronic and chemical advantages. First, the conjugated backbone of PmAP, structurally analogous to polyaniline, confers intrinsically high conductivity, enabling efficient electron transport across the sensing layer and thereby improving signal transduction and sensitivity.[26,27] Second, the pendant hydroxyl (–OH) groups distributed along the polymer chain introduce abundant sites for hydrogen bonding and other non-covalent interactions, which enhance the affinity toward α-lipoic acid (LA) and stabilize the analyte–polymer complex.[28,29] This dual functionality makes PmAP particularly attractive for electrochemical recognition processes. Furthermore, recent work by Mohanty *et al.*[30] demonstrated that PmAP can act as an efficient solid-state electron mediator in photocatalytic systems, highlighting its versatility in facilitating charge-transfer reactions. Therefore, we employed PmAP to fabricate disposable sensors by depositing cross-linked PmAP layers onto screen-printed gold electrodes (Au-SPEs) (Fig. 1). Electrochemical measurements were performed using a portable, wireless, hand-held potentiostat, employing techniques such as cyclic voltammetry (CV), differential pulse voltammetry (DPV), and electrochemical impedance spectroscopy (EIS). This innovative sensor effectively addresses the challenges in modern point-of-care (POC) diagnostics, while aligning with the ASSURED standards,[31] for reliability, affordability, and ease of use.

Experimental section

Synthesis of poly(*m*-aminophenol)

The synthesis of poly(*m*-aminophenol) (PmAP) was carried out by chemical oxidative polymerization of the monomer, *m*-aminophenol (mAP, 98%, Sigma-Aldrich), and a cross-linker, diphenylamine (DPA, ACS reagent, ≥99%, Sigma-Aldrich). This procedure was derived from a previously reported method for oxidative polymerization of mAP by Kar *et al.*[32] Briefly, 160 mg mAP and 248 mg DPA were dissolved in 10 mL of 0.1 M hydrochloric acid (HCl, locally obtained), and the solution was homogenized by ultrasonication for 30 min. Meanwhile, another solution was prepared by dissolving 410 mg of the initiator ammonium persulphate (APS, ACS reagent, ≥98.0%, Sigma-Aldrich) in 10 mL of 0.1 M HCl. Subsequently, the APS solution was added dropwise into the monomer and cross-linker solution.

This initiates the polymerization process, resulting in the formation of a black-colored reaction mixture, *i.e.*, a visual indication of PmAP formation. The resulting reaction mixture was stirred for 4 hours without heating. Afterward, the precipitates of PmAP formed were separated through centrifugation. The PmAP precipitates were washed multiple times with deionized water to remove unreacted species and HCl. Finally, the product was dried in air. A schematic showing the synthesis, fabrication, and application of a cross-linked PmAP/Au-SPE sensor is presented in Fig. 1.

Fabrication of disposable electrochemical devices

To obtain selective coatings on the electrode surface, 1 mg mL^{-1} of P*m*AP fine powder was dispersed in 0.5% polystyrene solution in THF. Polystyrene served as a binder to create stable coatings on the electrode surfaces. To ensure that the polymer powder was distributed uniformly throughout the mixture, the mixture was sonicated for 30 min. The P*m*AP suspension was applied on the screen-printed gold electrode, featuring gold working electrodes (WE), to develop a disposable P*m*AP/Au-SPE sensor. The gold WE disc had a diameter of 3 mm and a geometric area of 7.07 mm^2. The electrode surface was first cleaned by washing with water and methanol. Then, the surface of WE was drop-coated with 5 μL of P*m*AP suspension using a micropipette to fabricate the desired electrochemical LA sensor. The drop volume was optimized empirically to ensure full coverage of the working electrode and the formation of a uniform, adherent film. The fabricated devices were allowed to dry in air to evaporate the solvent, leaving behind a uniform P*m*AP film. Subsequently, the coated P*m*AP film was washed with deionized water to remove any residual impurities.

Characterization

The structural characterization of the polymer coating was conducted using an Agilent Technologies Cary 630 Fourier transform infrared (FTIR) spectrophotometer. The FTIR spectrum was recorded in the 4000–650 cm^{-1} range. The microstructure and surface morphology of the P*m*AP coating were investigated using an FEI Inspect S50 scanning electron microscope (SEM), and the images were further analyzed and processed using WSxM 4.0 Beta 9.3 software.[33]

Electrochemical sensor measurements

The electrochemical measurements were conducted by connecting an Au-SPE to a portable Sensit Smart potentiostat (PalmSense BV, The Netherlands). It offers wireless operation *via* the PSTouch app for Android smartphones or PSTrace software for Windows. To analyze the electrode coated with a P*m*AP layer, a standard redox solution in PBS buffer (pH = 7.4) was prepared by dissolving equimolar concentrations (2.5 mM) of $K_4[Fe(CN)_6]\cdot 3H_2O$ (ACS reagent, 98.5–102.0%, Sigma-Aldrich) and $K_3[Fe(CN)_6]$ (ACS reagent, ≥99.0%, Sigma-Aldrich) as the redox probe and 0.05 M KCl (ACS reagent, 99.0–100.5%, Sigma-Aldrich) as the electrolyte. Then, the standard redox solution was used to prepare a 1 mM stock solution of LA. Multiple analyte solutions with varying concentrations (1–500 μM) of LA were also prepared by the standard dilution method. A small amount of sodium hydroxide (NaOH, pellets, Sigma-Aldrich) was also added to help dissolve the LA. Similarly, solutions of various interfering analytes, such as glucose, glutamine, guanine, spermine, urea, uric acid, cholic acid, cholesterol, *etc.*, were also prepared for selectivity measurements.

Electrochemical impedance spectroscopy (EIS) was used to characterize the fabricated LA sensor and to determine the electrochemical characteristics of the corresponding polymeric coating. The impact of the scan rate (10–200 mV s^{-1}) was also investigated by cyclic voltammetry (CV) measurements. CV and differential pulse voltammetry (DPV) were employed to examine the electrochemical sensor response of disposable LA sensors. Voltammetric measurements were carried out in the potential range of −0.4 to +0.4 V at an optimized scan rate of 100 mV s^{-1}. A shift in the anodic peak currents (I_{pa}) as a function of the analyte concentration was used to determine the sensor response. The slope of the calibration curves was used to calculate the sensitivity of the P*m*AP/Au-SPE sensor. The limit of detection (LOD) and limit of quantification (LOQ) were then calculated using standard methods.[34] Afterward, the sensor's selectivity and operational stability were analyzed under identical conditions. All measurements were performed at 25 °C and in triplicate (at least) to obtain precise results along with the standard deviation.

Analysis of human serum

The P*m*AP/Au-SPE sensor was tested for its ability to detect LA in spiked blood serum samples to determine its real-world sensing applications. For this purpose, 2 mL samples of the blood serum were obtained from the University of the Punjab Health Centre. All the necessary protocols and institutional regulations were followed after the informed consent of the participating volunteers for the collection of serum samples. The study's ethical approval was obtained from the Institutional Ethics Review Board, University of the Punjab (Ref. D/111/FIMS). The serum samples were diluted to 6 mL using deionized water. The samples were centrifuged for 3 min at 4000 rpm, and the supernatant was recovered, followed by filtration using a sterile syringe filter (0.22 μm pore size). Centrifugation was used to separate the cellular components, such as red blood cells, white blood cells, and platelets, from serum, while filtration was employed to remove proteins and other biomacromolecules that could adsorb onto the sensor surface and block the active sites. Subsequently, further dilution (to 18 mL) of this pretreated serum solution was performed by the addition of a standard redox solution containing equimolar $[Fe(CN)_6]^{4-/3-}$ to set their overall concentration to 2.5 mM and KCl to set their concentration to 0.05 mM. The actual LA concentration ($C_{initial}$) was measured in each pretreated serum sample. Subsequently, each serum sample was spiked with 100 μM LA (C_{spiked}) for 5 serum samples, followed by measurements of the spiked serum samples to calculate the total concentrations (C_{total}) using CV at a scan rate of 100 mV s^{-1}. The recovery (%) was calculated as follows: $\{\text{recovery (\%)} = (C_{total} - C_{initial}) \times 100/C_{spiked}\}$. The mean values,

along with the standard deviation, are reported after the analysis of serum samples from five different volunteers.

Results and discussion

Spectroscopic characterization

The FTIR spectrum (Fig. 2a and b) exhibits sharp and intense peaks at 690 and 744 cm^{-1}, corresponding to out-of-plane bending vibrations of aromatic C–H bonds,[35] which confirms the presence of substituted benzene rings. Peaks at 1039 and 1165 cm^{-1} were attributed to C–O stretching vibrations from phenolic groups,[36] while the peaks at 1458, 1491, 1508, and 1560 cm^{-1} correspond to C=C stretching in aromatic rings and possible C=N stretching from imine linkages.[36,37] Less intense but well-defined peaks in the range of 874–1363 cm^{-1} are assigned to additional C–H bending, C–O, and C–N stretching vibrations.[38] The peaks at 3019 and 3038 cm^{-1} indicate aromatic C–H stretching.[39] A broad peak in the range of 3400–3100 cm^{-1} is observed, characteristic of O–H and N–H stretching vibrations, which confirms the presence of hydroxyl and amine groups involved in intermolecular hydrogen bonding.[38,40]

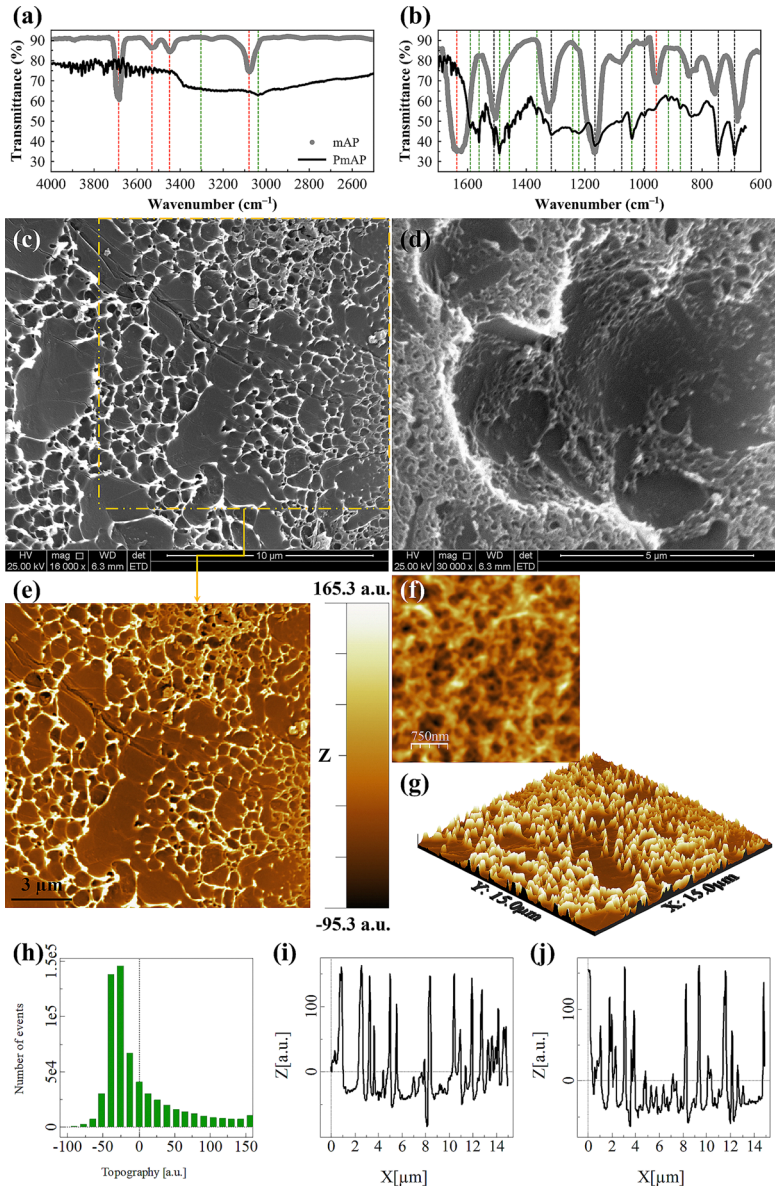

Fig. 2 Structural and morphological characterization of the synthesized P*m*AP. (a and b) FTIR spectra of the monomer (mAP) and the polymer (P*m*AP). Key spectral changes indicate successful polymerization: diminishing intensity of monomer peaks (red dashed lines), appearance of new vibrational modes (green dashed lines), and retained vibrations (black dashed lines). (c) and (d) Representative SEM images of the P*m*AP layer at (c) 16 000× and (d) 30 000× magnification, revealing a uniform and hierarchically porous morphology. Scale bars: (c) 10 µm and (d) 5 µm. (e) 2D and (g) 3D textured micrographs derived from SEM data, visualizing surface topography and porosity over a 15 × 15 μm^2 area. (f) A higher magnification view (3.75 × 3.75 μm^2). (h) Quantitative surface topography map corresponding to (g). (i) and (j) Surface height profiles along the (i) horizontal and (j) vertical lines passing through the center of (e), enabling quantitative analysis of surface roughness and pore dimensions.

The successful formation of P*m*AP was confirmed by the comparative FTIR spectrum of the mAP monomer, as presented in Fig. 2a and b. The spectrum of mAP shows characteristic sharp peaks, including O–H/N–H stretching (~3680 and 3075 cm^{-1}) and ring vibration modes (~1636 and 955 cm^{-1}). The diminishment of these monomer signatures and the emergence of new peaks in the P*m*AP spectrum provide direct evidence of polymer formation. The band at ~1040 cm^{-1} is attributed to C–O stretching of the phenolic group within the polymer chain. The features between 1450 and 1600 cm^{-1}, notably at ~1560 and ~1590 cm^{-1}, are assigned to the C=C and C=N stretching vibrations of the quinoid and benzenoid rings, confirming the development of a conjugated polymer structure.[1,28,32] These spectral features confirm the successful polymerization and cross-linking of P*m*AP, which highlights the presence of aromatic, hydroxyl, amine, and imine functional groups.

Microstructure and surface morphology

The SEM analysis (Fig. 2c and d) provides a detailed visualization of the surface morphology of the P*m*AP interface layer fabricated on the Au-SPE. The micrographs reveal a uniform and hierarchically porous structure, characterized by the presence of both small and large pores, which appear as dark voids in the images (Fig. 2e and f). These pores likely form due to the evaporation of solvent molecules during the fabrication process. The presence of this interconnected porous network significantly enhances the effective surface area and is expected to promote greater interaction with the analyte and facilitate electron transfer.[41] To further explore the surface architecture, a 3D textured SEM image (Fig. 2g) offers an enhanced visualization of the microstructure, highlighting variations in topography. The roughness analysis (Fig. 2h) quantifies these variations, revealing a root-mean-square roughness of 50.0 nm. Additionally, a high kurtosis value of 4.76 indicates a leptokurtic surface, which suggests sharper peaks and deeper valleys, contributing to an increased electrochemically active surface area and improved analyte adsorption.[42] Furthermore, the surface profile analysis (Fig. 2i and j) confirms the presence of a well-distributed porous morphology, which may promote enhanced mass transport and efficient electron transfer at the electrode interface. This structural integrity and surface roughness collectively enhance the sensor's sensitivity and performance in electrochemical applications.

Electrochemical characterization

The EIS response of the unmodified Au-SPE is characteristic of a single, non-ideal interfacial relaxation superimposed on a low-frequency diffusion-like process (Fig. 3a). In the Nyquist representation, a depressed semicircle at mid–high frequencies ($R_{ct} \approx 3589 \pm 123\ \Omega$; $\chi^2 = 0.0091$) is observed after a small solution resistance ($R_s \approx 87.6\ \Omega$), while the low-frequency region shows the upward tail that was modelled by a finite Warburg element ($W_1 \approx 1.65\ k\Omega$) in a modified Randles circuit. The fitted constant-phase element ($Q_1 \approx 0.586\ \mu S\ s^n$) has an exponent $n \approx 0.943$, indicating that the capacitive behavior is

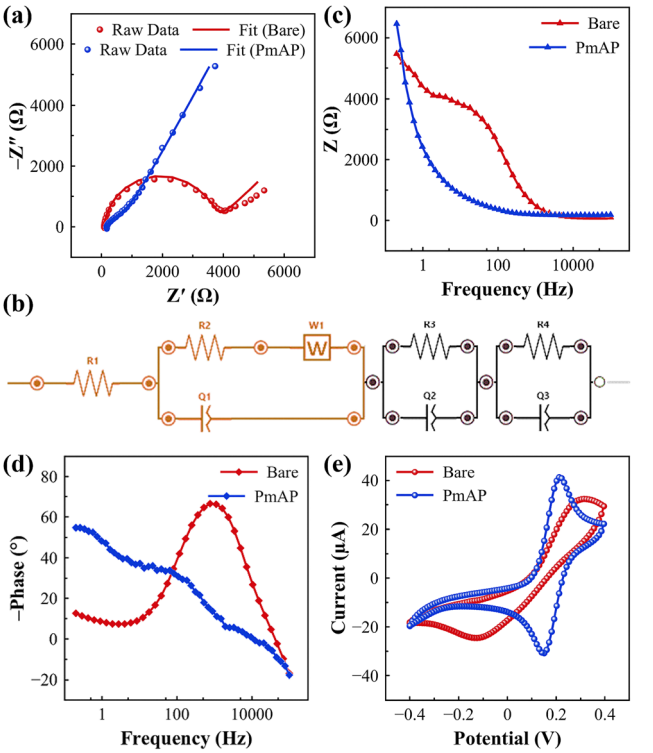

Fig. 3 EIS analysis: (a) Nyquist plots of the bare and P*m*AP-modified electrodes and (b) the modified Randles circuit model employed to model EIS data of the P*m*AP-modified electrode. (c) Bode magnitude plots and (d) Bode phase angle plots of the bare and P*m*AP-modified electrodes. (e) CV scans of the bare and P*m*AP-modified electrodes. The electrochemical measurements were conducted in a standard redox solution containing 0.05 M KCl and 2.5 mM $[Fe(CN)_6]^{4-/3-}$ in PBS (pH 7.4) at 25 °C.

close to ideal but still subject to modest surface heterogeneity. The Bode plots corroborate this assignment (Fig. 3c and d): a single dominant phase maximum (broadened rather than sharp) and a gradual decay of $|Z|$ with frequency point to distributed interfacial capacitance together with mass-transport limitations at long times.

The EIS analysis provides deeper insights into the interfacial charge transport processes and the role of the porous polymeric film in governing electron transfer dynamics. The Nyquist plot of the P*m*AP-modified Au-SPE (Fig. 3a) exhibits a well-defined semicircular domain at high to mid frequencies, followed by a steep rise at lower frequencies, indicative of the coexistence of charge-transfer resistance, capacitive elements, and diffusion contributions. Fitting of the data to the selected equivalent circuit model (Fig. 3b), which incorporates resistive, constant phase, and transmission line elements, yielded excellent agreement with a χ^2 value of 0.0086, confirming the robustness of the fit. The uncompensated solution resistance ($R_s = 38.2\ \Omega$) is reasonably low, reflecting good ionic conductivity of the electrolyte and efficient cell configuration.[43] The dominant charge transfer resistance associated with the P*m*AP/Au-SPE interface is reflected in $R_{ct} = 1074 \pm 12\ \Omega$, a value that, while significant, is much smaller than that of the bare Au-SPE ($R_{ct} \approx 3589 \pm 123\ \Omega$) discussed earlier, suggesting that the porous P*m*AP film provides

efficient pathways for charge transport across the electrode/electrolyte boundary.[44]

The equivalent circuit also incorporates constant phase elements (Fig. 3b), which account for the non-ideal capacitive response arising from surface roughness and the heterogeneous distribution of active sites within the P*m*AP matrix. The depressed semicircle observed in the Nyquist spectrum and the non-integer values of the $n \approx 0.675$ exponents associated with the CPEs confirm that the interface cannot be described as an ideal capacitor but rather exhibits distributed capacitance linked to the hierarchical porosity of the polymer.[45] In particular, Q_1, coupled with the large transmission line element (T_1), captures the porous, thin-film nature of the P*m*AP coating, consistent with the morphological evidence of highly porous domains from SEM.

The Bode plot further supports this interpretation (Fig. 3c and d). The gradual decay of impedance magnitude with frequency and the broad phase angle response, which does not approach an ideal −90°, reflect the coexistence of capacitive and resistive elements distributed across the porous interface. The broadening of the phase peak is diagnostic of multiple relaxation processes arising from electron transfer at different domains of the P*m*AP network and the ionic transport through its porous structure.[46] The inclusion of transmission line elements in the circuit fitting reinforces this notion, as such elements are typically associated with porous electrodes where distributed ionic conduction and interfacial charging occur simultaneously.

The CV comparison between the bare and P*m*AP-modified Au-SPEs in 2.5 mM $[Fe(CN)_6]^{3-/4-}$ (0.05 M KCl, PBS, 100 mV s^{-1}) highlights the pronounced role of the polymeric film in facilitating interfacial charge transfer (Fig. 3e). The bare electrode exhibits an anodic peak current (I_{pa}) of 32.39 μA, serving as the baseline for comparison. This relatively low current reflects the unmodified electrode's limited active surface area and less efficient electron transfer kinetics. Upon modification with P*m*AP, the I_{pa} increases significantly to 41.28 μA, indicating enhanced electrochemical activity, which is attributed to the increased effective surface area and improved electron transfer rate.

Mechanism of redox processes

The nature of the electrochemical processes at the electrode–electrolyte interface can be assessed using the CV scans obtained at different scan rates (ν), spanning 10–200 mV s^{-1} (Fig. 4a). With increasing scan rates, the P*m*AP/Au-SPE sensor shows a successive increase and decrease in anodic (I_{pa}) and cathodic (I_{pc}) peak currents, respectively, demonstrating a linear dependence of the redox process on the applied ν (Fig. 4b), with an R^2 value of 0.995. This refers to the adsorption-controlled redox processes.[47] The correlation between the peak currents and the square root of scan rates ($\nu^{1/2}$) is also linear with R^2 equal to 0.971 for the P*m*AP/Au-SPE sensor, as shown in Fig. 4c, which reflects the diffusion-controlled mechanism,[48,49] especially in the lower scan rate range. The log–log plot (Fig. 4d) provides further evidence for the mechanism of the redox processes occurring at the electrode–electrolyte interface. The linear relationship between log(I_{pa}) and log(ν) with a slope value of 0.81 suggests

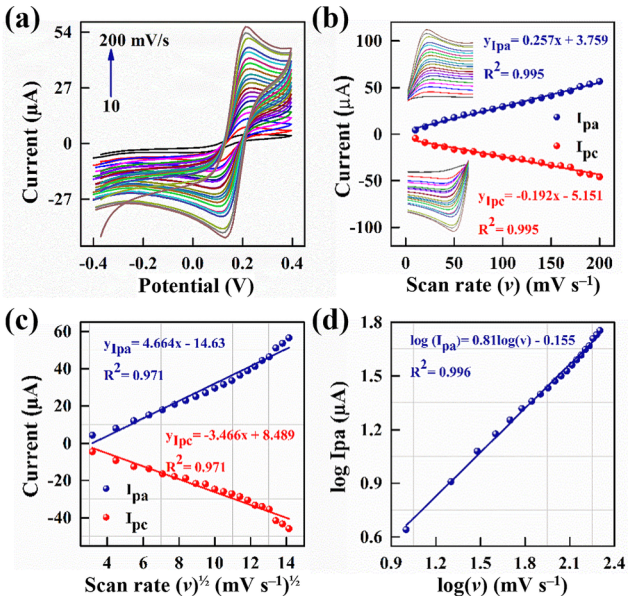

Fig. 4 (a) Cyclic voltammograms of the P*m*AP/Au-SPE sensor at different scan rates (10–200 mV s^{-1}) in a standard redox solution. (b) and (c) Linear regression plots, showing the relationship of redox peak currents with (b) the scan rate (ν) and (c) the square root of the scan rate ($\nu^{\frac{1}{2}}$). (d) Log–log plot: the logarithm of I_{pa} plotted as a function of the logarithm of ν. The corresponding linear regression equations are also provided in (b)–(d). All measurements were conducted in a standard redox solution containing 0.05 M KCl and 2.5 mM $[Fe(CN)_6]^{4-/3-}$ in PBS (pH 7.4) at 25 °C.

mixed redox mechanisms, *i.e.*, the redox processes are predominantly adsorption-controlled with little contribution from the diffusion-controlled process.[50,51]

This interpretation is further supported by the peak-to-peak separation (ΔE_p), which was 81.7 mV and, unusually, decreased with increasing ν. Unlike classical diffusion-controlled systems, where ΔE_p broadens at higher scan rates, this trend is characteristic of thin-layer or surface-confined electrochemistry. The hierarchical porous P*m*AP architecture (Fig. 2c and d) likely entraps $[Fe(CN)_6]^{3-/4-}$ species, facilitating their rapid access to electroactive sites and accelerating electron-transfer kinetics. Together, these results indicate that P*m*AP modification drives the system toward quasi-reversible to nearly reversible behavior, with surface-confined contributions becoming increasingly dominant at higher scan rates.

Electrochemical properties

The electroactive surface area (A_{elec}) of the P*m*AP-modified electrodes was estimated from EIS data. The double-layer capacitance ($C_{dl,eff}$) was obtained by fitting the EIS data to a modified Randles equivalent circuit, containing a constant phase element (CPE), to account for the surface inhomogeneity and porosity of the P*m*AP film (Fig. 3b). The effective $C_{dl,eff}$ was calculated from the fitted CPE parameters (Q and n) and the charge-transfer resistance (R_{ct}) using Brug's formula for a non-ideal interface (eqn (1)):[52]

$$C_{dl,eff} = Q^{\frac{1}{n}} R_{ct}^{\frac{(1-n)}{n}} \quad (1)$$

where Q is the CPE constant, n is the CPE exponent ($0 \leq n \leq 1$), and R_{ct} is the charge-transfer resistance. The specific capacitance (C_s) for a perfectly smooth, unmodified polycrystalline gold electrode was taken as a standard literature value of 20 μF cm^2.[46,53] A_{elec} was then calculated using the relation (eqn (2)):[54]

$$A_{elec} = \frac{C_{dl,eff}}{C_s} \quad (2)$$

This method yields a value of 0.564 cm^2, which is significantly larger than the geometric area (0.071 cm^2). This notable difference, corresponding to a roughness factor of ~7.94, indicates that the P*m*AP modification creates a highly rough and porous surface structure that greatly facilitates charge transport.

The apparent surface coverage (Γ_{app}, mol cm^{-2}) of the electroactive $[Fe(CN)_6]^{4-/3-}$ species was estimated using Laviron's equation for adsorbed species (eqn (3)).[55,56]

$$I_p = n^2F^2A_{elec}\Gamma_{app}\nu/4RT \quad (3)$$

While the redox probe is not permanently immobilized, its interaction with the porous P*m*AP film at slower scan rates exhibits adsorption-like behavior, justifying the use of this model. For the calculation, the number of electrons transferred (n) was 1, the Faraday constant (F) was 96 485 C mol^{-1}, the universal gas constant (R) was 8.314 J mol^{-1} K^{-1}, and the temperature (T) was 298 K. The calculated Γ_{app} was 4.85 × 10^{-10} mol cm^{-2}, indicating a high density of accessible redox-active sites. For redox-active species immobilized or adsorbed on an electrode, this value is typically interpreted as a dense and effective surface coverage.[57,58] This suggests that the modification process successfully immobilized a significant number of electroactive sites, further supporting the large electroactive area observed.

The heterogeneous electron transfer rate constant (K^0, cm s^{-1}) was calculated from the charge-transfer resistance (R_{ct}) obtained from the fitted EIS data (Fig. 3b), the electroactive area (A_{elec}), and the concentration of the redox probe (C, mol cm^{-3}) using eqn (4):[59,60]

$$K^0 = RT/n^2F^2R_{ct}A_{elec}C \quad (4)$$

The concentration (C) of the $[Fe(CN)_6]^{4-/3-}$ solution was 2.5 mM (2.5 × 10^{-6} mol cm^{-3}). The value of K^0 was determined to be 1.76 × 10^{-4} cm s^{-1}, indicating moderately fast electron transfer kinetics.[61,62] This improvement is attributed to the increased electroactive surface area, efficient charge transfer pathways, and the conductive nature of the polymer. The rough and porous structure of the modified electrode also provides more active sites, reducing charge transfer resistance and facilitating faster electron exchange.

Electrochemical sensor measurements

CV analysis was performed to investigate the electrochemical response of the P*m*AP/Au-SPE sensor across a range of LA concentrations (1–400 μM) in a standard redox solution (pH 7.4) at a scan rate of 100 mV s^{-1}. The results, presented in Fig. 5, reveal a progressive decrease in anodic peak current (I_{pa}) with increasing LA concentration (Fig. 5a). This trend suggests that LA actively modulates the redox behavior of the electrode surface, likely through specific interactions with the P*m*AP interface, which influences charge transfer dynamics and alters the electrochemical response, as discussed later. The calibration curve (Fig. 5b) demonstrates a linear relationship between the I_{pa} and LA concentration, with a strong correlation coefficient (R^2 = 0.988). The slope of the calibration curve is calculated to be 0.03 μA μM^{-1}, highlighting the sensor's sensitivity to LA concentration changes. This high degree of linearity and electrochemical responsiveness suggest the strong capability of the P*m*AP/Au-SPE sensor for precise and reliable LA detection.

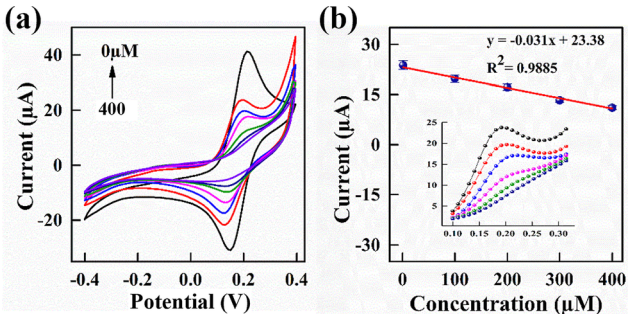

Fig. 5 (a) Cyclic voltammograms of the P*m*AP/Au-SPE sensor towards different LA concentrations (1–400 μM) in a standard redox solution. (b) A calibration plot of current response (I_{pa}) *vs.* LA concentration. The corresponding linear regression equation is given in (b). All measurements were conducted in a standard redox solution containing 0.05 M KCl and 2.5 mM $[Fe(CN)_6]^{4-/3-}$ in PBS (pH 7.4) at 25 °C and at 100 mV s^{-1}.

LA sensing mechanism

The detection of LA is achieved through an indirect "blocking" mechanism, as revealed through CV measurements. The process is as follows: (i) the P*m*AP/Au-SPE sensor provides a strong, stable current response from the reversible oxidation and reduction of the $[Fe(CN)_6]^{4-/3-}$ probe in solution. (ii) When LA is added, its molecules selectively adsorb onto the active sites of the porous P*m*AP interface. We propose that this occurs *via* hydrogen bonding between the pendant –OH groups of P*m*AP and the functional groups of LA. (iii) The adsorbed LA molecules act as a non-conductive layer, physically blocking the access of the $[Fe(CN)_6]^{4-/3-}$ anions to the electroactive surface of the sensor.[63,64] (iv) This blockage impedes the electron transfer process, leading to a quantifiable decrease in the peak current. (v) The degree of current attenuation is directly proportional to the amount of LA adsorbed, which in turn is dependent on its concentration in solution. This relationship provides the calibration curve shown in Fig. 5b.

The mixed adsorption–diffusion controlled process of the redox probe at the P*m*AP interface (as established in Fig. 4) is a crucial prerequisite for this mechanism. The significant contribution from surface-confined species indicates that the sensor's response is highly sensitive to any obstruction of the active sites, amplifying the blocking effect caused by LA adsorption. This phenomenon is presented in Fig. 6, which illustrates

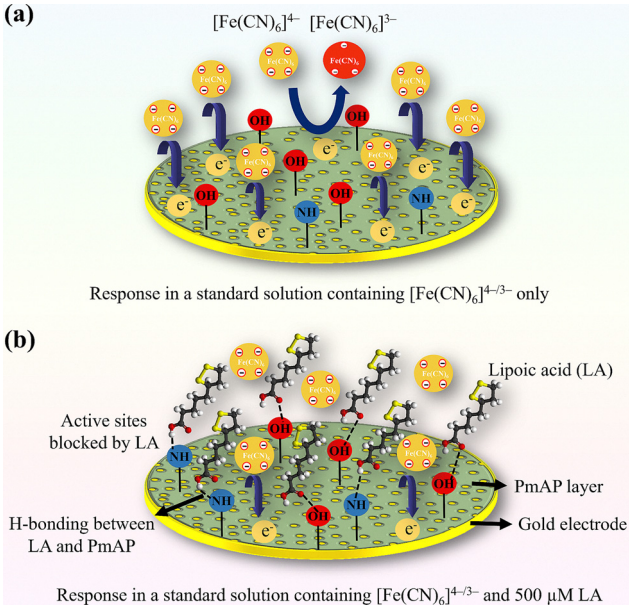

Fig. 6 LA sensing mechanism: (a) when LA is absent, the P*m*AP/Au-SPE sensor shows a high peak current in a standard redox solution containing $[Fe(CN)_6]^{4-/3-}$ due to the increased accessibility of $[Fe(CN)_6]^{4-/3-}$ to the surface. (b) In the presence of LA in the same redox solution, the P*m*AP/Au-SPE surface is blocked by the selective binding of LA, which limits the accessibility of $[Fe(CN)_6]^{4-/3-}$ to the surface, thereby hindering charge transfer and decreasing the current.

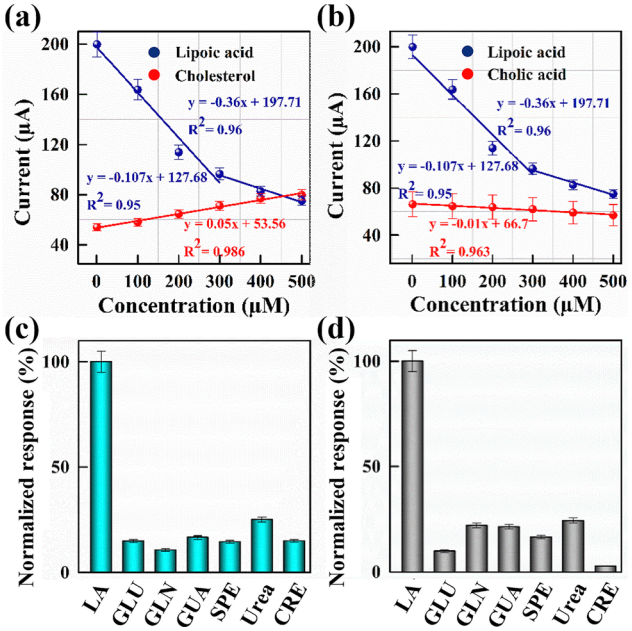

Fig. 8 (a and b) Calibration plots showing the current response of the P*m*AP/Au-SPE sensor toward different concentrations (1–500 μM) of (a) cholesterol, and (b) cholic acid, in comparison with LA. Normalized response of the P*m*AP/Au-SPE sensor, estimated from the respective (c) CV and (d) DPV scans, toward different metabolites, including LA (lipoic acid), GLU (glucose), GLN (glutamine), GUA (guanine), SPE (spermine), urea, and CRE (creatinine). All measurements were conducted in a standard redox solution containing 0.05 M KCl and 2.5 mM $[Fe(CN)_6]^{4-/3-}$ in PBS (pH 7.4) at 25 °C and 100 mV s^{-1}.

the unimpeded electron transfer in the absence of LA and the restricted electron transfer when LA is present in the redox solution.

Differential pulse voltammetry

DPV analysis was performed to further validate the sensitivity of the P*m*AP/Au-SPE sensor, as it offers more reliable results.[65] The results are presented in Fig. 7a and b, showing a decrease in peak current with increasing LA concentration. From the slope of the calibration plot of current density *vs.* LA concentration (Fig. 7c), the sensitivity of the P*m*AP/Au-SPE sensor is determined to be 4.77 μA cm^{-2} μM^{-1} (~0.36 μA μM^{-1}) in the linear detection range of 1–300 μM and 1.47 μA cm^{-2} μM^{-1} (~0.11 μA μM^{-1}) in the detection range of 300–500 μM. This higher sensitivity suggests that the P*m*AP/Au-SPE sensor is more effective at detecting changes in LA concentration due to the enhanced interaction between LA and the P*m*AP interface, as discussed above. A decrease in sensitivity at higher concentrations also suggests the saturation of sensor response,

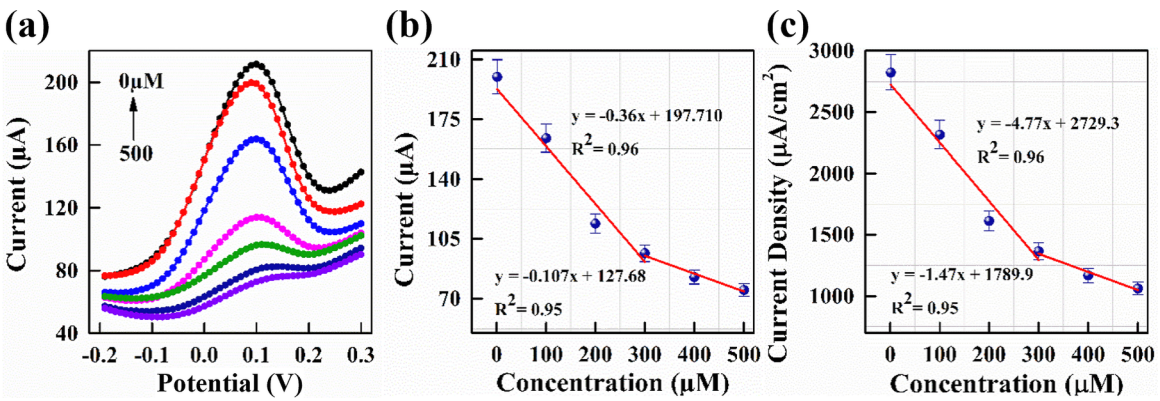

Fig. 7 (a) DPV scans of the P*m*AP/Au-SPE sensor towards different LA concentrations (1–500 μM) in a standard redox solution. (b) A calibration plot of current response (I_{pa}) *vs.* LA concentration. (c) A calibration plot of current density *vs.* LA concentration. The corresponding linear regression equations are given in (b and c). All measurements were conducted in a standard redox solution containing 0.05 M KCl and 2.5 mM $[Fe(CN)_6]^{4-/3-}$ in PBS (pH 7.4) at 25 °C and 100 mV s^{-1}.

likely due to the blockage of interaction sites for $[Fe(CN)_6]^{4-/3-}$ redox species by LA adsorption, thereby inhibiting charge transfer.[63] Hence, it also validates the LA sensing mechanism, as discussed above. The limit of detection (LOD) and limit of quantification (LOQ) are calculated using the following formula:[66] LOD = 3.3 σ/S and LOQ = 10σ/S. Thus, the LOD and LOQ of the P*m*AP/Au-SPE sensor are found to be 0.43 μM and 1.30 μM, respectively. These parameters were evaluated against the findings from recent studies on electrochemical LA sensors, as discussed later.

Selectivity experiments

The selectivity of the P*m*AP/Au-SPE sensor is examined using 1–500 μM concentrations of competitor analytes: cholesterol (Fig. 8a) and cholic acid (Fig. 8b). Compared to LA, the sensor displays negligible current response toward cholesterol and cholic acid, with 7-fold and 36-fold lower sensitivity toward cholesterol and cholic acid, respectively. In addition, to assess selectivity, the sensor's response is tested against several metabolites present in human serum, including glucose, glutamine, guanine, spermine, urea, and creatinine. These analytes were selected to represent the complex matrix (serum) in which LA detection is critical for diagnosing NELL-1 MN. The bar graph illustrated in Fig. 8c and d demonstrates the P*m*AP/Au-SPE sensor's normalized response toward the highest concentrations of these analytes. The sensor exhibits a significantly higher response to LA compared to other analytes, highlighting its excellent selectivity and specificity toward LA. This selectivity of the P*m*AP/Au-SPE sensor can be attributed to the effective interaction between the functional groups in LA and the active sites present on P*m*AP, enabling the selective recognition of LA and minimizing interference from other analytes. These findings confirm the sensor's excellent specificity for LA and its compatibility with applications requiring precise detection of LA.

Analysis of human serum samples

The analysis of LA in real samples, such as human serum, is critical for the development of cost-effective diagnostic tools. Human serum, being an ideal physiological fluid for LA detection, provides valuable insights into normal kidney function and related metabolic processes. To explore the potential of the P*m*AP/Au-SPE sensor for practical applications, a disposable P*m*AP/Au-SPE sensor was employed for LA quantification in serum samples obtained from five different individuals. Fig. 9a presents a schematic of the human serum collection, pretreatment, and analysis using a disposable P*m*AP/Au-SPE sensor. The human serum samples were pretreated and diluted to

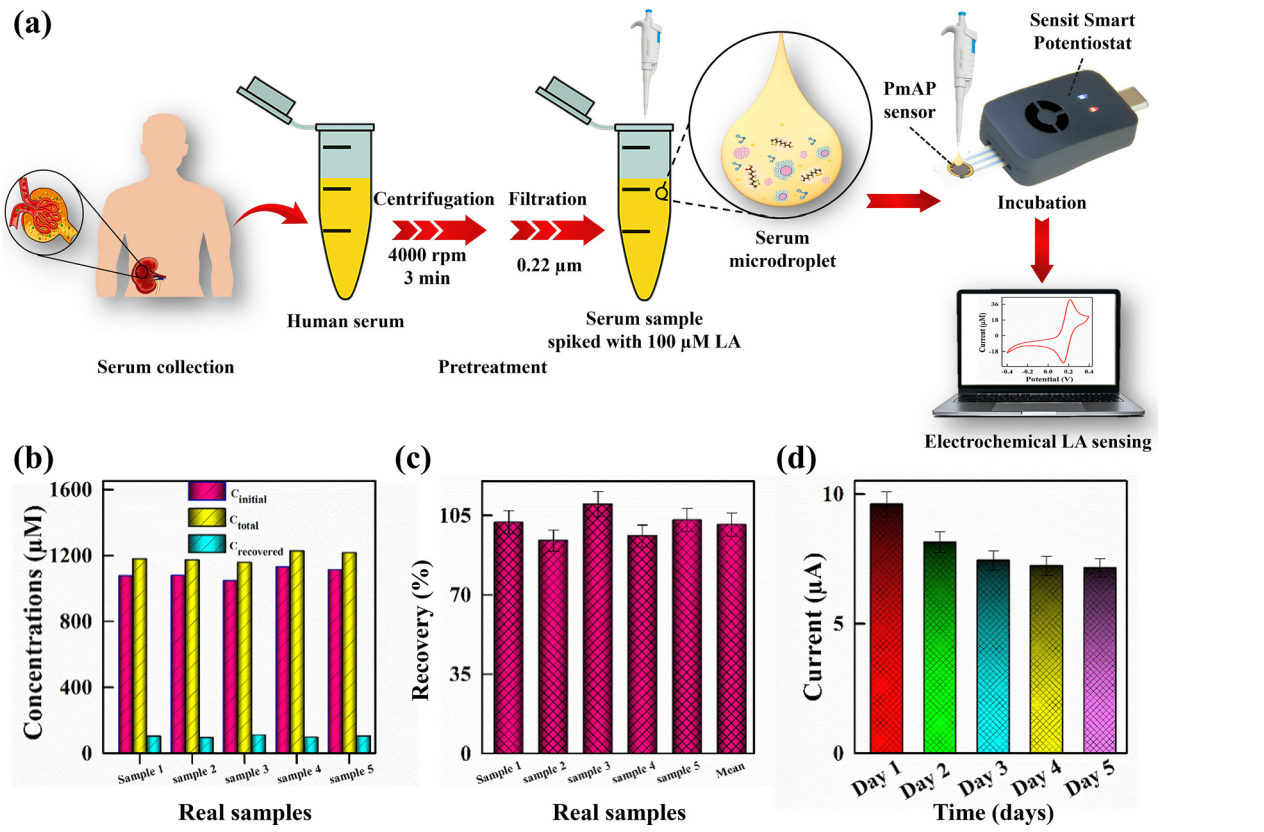

Fig. 9 (a) A schematic showing serum collection, pretreatment, and analysis using a disposable P*m*AP/Au-SPE sensor for LA detection. (b) The analysis of serum samples, obtained from five different individuals, before and after spiking with a known concentration (100 μM) of LA. (c) The calculated percent recovery for five samples, along with their mean, after spiking 100 μM LA. (d) The operational stability of the P*m*AP/Au-SPE sensor toward 500 μM LA over 5 days of continuous electrochemical sensor measurements.

Table 1 Recovery data for the determination of α-lipoic acid (LA) in spiked human serum samples using the P*m*AP/Au-SPE sensor (n = 3)

	Concentration (C, μM)			
Human serum	Initial	Spiked	Total found	Recovery (%)
Sample 1	1076	100	1178	102 ± 5.0
Sample 2	1077	100	1171	94 ± 4.8
Sample 3	1046	100	1156	110 ± 5.4
Sample 4	1129	100	1225	96 ± 4.7
Sample 5	1112	100	1215	103 ± 5.1

mitigate potential matrix effects. The complex serum matrix, containing proteins and other biomacromolecules, can cause electrode fouling and alter diffusion kinetics, suppressing the electrochemical signal. Dilution reduces the concentration of these interferents and the sample viscosity, thereby minimizing fouling and facilitating mass transport of the analyte to the electrode surface.

The pretreated serum samples were directly tested for the quantification of LA, yielding 1.088 ± 0.033 mM LA. This insight allows the assessment of the sensor's ability to accurately detect and recover LA in a complex biological fluid. Subsequently, five different serum samples were spiked with a 100 μM concentration of LA, and the recovery results are reported in Fig. 9b and c and Table 1. The recovery (%) of spiked LA concentrations is calculated by using the following formula (eqn (5)):[67]

$$\text{Recovery}\,(\%) = \frac{C_{\text{total}} - C_{\text{initial}}}{C_{\text{spiked}}} \times 100 \qquad (5)$$

The P*m*AP/Au-SPE sensor demonstrates excellent recovery of spiked LA concentrations, showing a mean value of 101 ± 6.32%, which indicates its high precision and reliability for LA quantification in real-world applications. It is important to note that the interpretation of LA levels can be complicated by exogenous intake from nutritional supplements and variations due to other metabolic conditions. Therefore, clinical correlation and patient history are essential for contextualizing LA measurements. The primary utility of this sensor lies in longitudinal monitoring of LA trends in patients to track disease onset, activity, and/or treatment response, rather than in a standalone diagnostic application.

Repeatability and operational stability

The inter-electrode reproducibility (repeatability) was evaluated by testing three independently prepared P*m*AP/Au-SPE sensors against a 100 μM LA solution. The resulting current responses showed a relative standard deviation (RSD) of 4.1%, demonstrating excellent manufacturing consistency. Furthermore, the operational stability of the P*m*AP/Au-SPE sensor was assessed to realize the robustness of the P*m*AP interface under continuous operation. The sensor's performance was analyzed by testing a 500 μM LA concentration over five consecutive days using CV. As presented in Fig. 9d, the sensor retained approximately 74% of its initial response after five days of reuse. This stability is attributed to the robust nature of the P*m*AP interface, offering structural integrity and resistance to contamination and degradation even after prolonged operation. These findings corroborate the P*m*AP/Au-SPE sensor's suitability for diagnostic applications, particularly NELL-1 MN, through LA analysis.

State-of-the-art comparison

The P*m*AP/Au-SPE sensor demonstrates strong analytical performance, as highlighted by its wide detection range, competitive sensitivity, and low detection limit when compared with previously reported electrochemical sensors for LA quantification (Table 2). These advantages, along with good selectivity and practical applicability, position it as a promising alternative to conventional detection methods. However, a limitation of the present study lies in the relatively sparse data points used for calibration curve construction, which, while still yielding excellent linearity and correlation coefficients, could be further strengthened by higher data density to enhance statistical confidence in the linear ranges. Despite this, the high recovery rates in human serum confirm the sensor's robustness and practical potential for reliable LA quantification, and the collective results establish P*m*AP/Au-SPE as a viable and scalable platform for future biosensing applications.

Table 2 A comparison of the P*m*AP/Au-SPE sensor's performance with previously reported electrochemical LA sensors

Materials	Method	Detection range (μM)	Sensitivity (μA μM^{-1})	LOD (μM)	Ref.
PV-CS/f-MWCNTs/GCE	DPV	0–3000	0.0466	0.012	68
Diamond spray-polished GCE	DPV	2.5–75	0.0012	1.8	69
B-doped diamond electrode	DPV	0.3–105	0.0236	0.088	70
CoPc/PG	CV	1.99–263	—	0.25	71
	DPV	0.499–19.6		0.0034	
SnO_2-CTPPB/GCE	DPV	0.5–50	0.034	0.13	72
		50–400	0.8	0.43	
MWCNTs/GCE	LSV	26–180	17.7	19.0	73
MWCNT/PIN/Ti_2O_3/GCE	DPV	0.39–115.8	0.460[a]	0.012	74
P*m*AP/Au-SPE	CV	1–400	0.031	0.193	This
	DPV	1–300	0.360	0.430	work

Note: Au-SPE – screen-printed gold electrode; CoPc – cobalt phthalocyanine; CTPPB – cetyltriphenylphosphonium bromide; CV – cyclic voltammetry; DPV – differential pulse voltammetry; GCE – glassy carbon electrode; LSV – linear sweep voltammetry; MWCNTs – multi-walled carbon nanotubes; PG – pyrolytic graphite; PIN – polyindole; P*m*AP – poly(*m*-aminophenol); PV-CS – poly(vanillin-*co*-chitosan). [a] Converted from 6.39 μA cm^{-2} μM^{-1} using the area of the electrode (0.0721 cm^2).[74]

Conclusion

In summary, this study reveals the development and analysis of a disposable, cost-efficient electrochemical LA sensor based on the conducting P*m*AP polymer. The electrochemical evaluation, including CV, DPV, and EIS techniques, shows the sensor's exceptional properties. EIS shows excellent charge transfer with minimal resistance at the electrode–electrolyte interface. DPV reveals high sensitivity (4.77 μA cm^{-2} μM^{-1}) with a limit of detection (LOD) of 0.43 μM, offering the rapid identification of trace LA levels in human serum. In addition, it shows considerable selectivity, allowing minimal interference from common metabolites. Although designed as a disposable device, the sensor maintains over 74% of its initial response after 5 days of continuous reuse, indicating the robustness of P*m*AP. The sensor enables meticulous LA recovery in real serum samples, yielding a 101 ± 6.32% recovery of LA. However, the key challenges that remain unresolved include using P*m*AP/Au-SPE sensors in untreated serum samples and ensuring long-term storage stability. Nonetheless, the P*m*AP/Au-SPE sensor is an outstanding POC diagnostic device for monitoring trace LA levels and routine monitoring of kidney function through serum droplet analysis.

Conflicts of interest

The authors declare no conflicts of interest.

Data availability

The data that support the findings of this study are included within the article.

Acknowledgements

A. A. gratefully acknowledges the partial provision of research facilities by the University of Hafr Al Batin and the Ministry of Education, KSA and characterization support provided by Dr Amir Habib. K. B. acknowledges the use of generative AI to improve the readability and language of the manuscript.

References

1 S. Narayanasami, N. Vijayakumar, M. Trivedi, A. Sekar, S. Sulaiman, S. Nayak, N. Inamdar, S. Sharma, R. Parthasarathy, V. Kadam, V. Keskar, S. Bagai, A. Kumar, B. Reen, A. Kurien, A. Sharma, D. Khullar, B. Hafeeq, A. Krishnakumar and R. Ramachandran, *Kidney Int. Rep.*, 2024, **9**, 1513–1516.
2 S. Zhou, F. Meng, S. Yue, H. Li, L. Zhang and T. Wang, *Clin. Kidney J.*, 2023, **16**, 756–759.
3 S. Sethi, *Clin. Kidney J.*, 2023, **16**, 442–446.
4 P. Ronco, L. Beck, H. Debiec, F. C. Fervenza, F. F. Hou, V. Jha, S. Sethi, A. Tong, M. Vivarelli and J. Wetzels, *Nat. Rev. Dis. Primer*, 2021, **7**, 69.
5 P. Kashiv, S. Malde, S. Gupta, S. Dubey, K. N. Sejpal, T. Pawar, V. Mahajan, P. Gurjar, A. Pasari and M. Balwani, *Cureus*, 2024, **16**, e61230.
6 T. N. Caza and C. P. Larsen, *Kidney Int.*, 2022, **101**, 418–419.
7 R. Nassar, S. A. Kadhem and M. Shakir, *Kans. J. Med.*, 2023, **16**, 297–298.
8 N. A. Yudhaswara, A. R. Prijanti and M. Sadikin, *Acta Biochim. Indones.*, 2020, **3**, 14–22.
9 G. K. Deepthi, D. T. E. Divakar, N. B. Murthy and D. Pavankumar, *Int. J. Eng. Res. Technol.*, 2013, **1**, 1–6.
10 G. Chwatko, M. Krawczyk, M. Iciek, A. Kamińska, A. Bilska-Wilkosz, B. Marcykiewicz and R. Głowacki, *Arab. J. Chem.*, 2019, **12**, 4878–4886.
11 H. Kataoka, N. Hirabayashi and M. Makita, *Methods in Enzymology*, Academic Press, 1997, vol. 279, pp. 166–176.
12 G. K. Ziyatdinova, G. K. Budnikov and V. I. Pogorel'tsev, *J. Anal. Chem.*, 2004, **59**, 288–290.
13 H. Bhardwaj, Archana, A. Noumani, J. K. Himanshu, S. Chakravorty and P. R. Solanki, *Mater. Adv.*, 2024, **5**, 475–503.
14 S. S. Paramasivam, S. A. Mariappan, N. K. Sethy and P. Manickam, *Mater. Adv.*, 2023, **4**, 6223–6232.
15 M. Zahran, *Mater. Adv.*, 2024, **5**, 68–82.
16 M. Marin, C. Lete, B. N. Manolescu and S. Lupu, *J. Electroanal. Chem.*, 2014, **729**, 128–134.
17 Ö. Güngör, B. Kiliç, T. Seren Karasürmeli, İ. Özcan and S. Köytepe, *Measurement*, 2021, **182**, 109752.
18 S. Titretir Duran, C. Ben Ali Hassine, M. Burç and Ö. Güngör, *Anal. Bioanal. Electrochem.*, 2020, **12**, 857–869.
19 V. Karabozhikova and V. Tsakova, *Coatings*, 2023, **13**, 2014.
20 Á. Terán-Alcocer, F. Bravo-Plascencia, C. Cevallos-Morillo and A. Palma-Cando, *Nanomaterials*, 2021, **11**, 252.
21 Y. Pan, J. Zhang, X. Guo, Y. Li, L. Li and L. Pan, *Polymers*, 2024, **16**, 1597.
22 G. Deffo, C. G. Fotsop, M. C. D. Ngaha, S. G. Fogang, L. A. Vomo, B. W. Nkuigoua, C. A. Shella, A. V. Somba, T. F. N. Tene, I. K. Tchummegne, E. Njanja, I. K. Tonlé, P. Puzari and E. Ngameni, *Mater. Adv.*, 2024, **5**, 3683–3695.
23 N. Sharma, A. Singh, N. Kumar, A. Tiwari, M. Lal and S. Arya, *J. Mater. Sci.*, 2024, **59**, 6206–6244.
24 K. Shehzad, A. Ul-Haq, S. Ahmad, M. Mumtaz, T. Hussain, A. Mujahid, A. T. Shah, M. Y. Choudhry, I. Khokhar, S. Ul-Hassan, F. Nawaz, F. Ur Rahman, Y. Butt and M. Pervaiz, *J. Mater. Sci.*, 2013, **48**, 3737–3744.
25 T. Hussain, S. Jabeen, K. Shehzad, A. Mujahid, M. N. Ahmad, Z. H. Farooqi and M. H. Raza, *Polym. Compos.*, 2018, **39**, E1346–E1353.
26 P. Kar, N. C. Pradhan and B. Adhikari, *Mater. Chem. Phys.*, 2008, **111**, 59–64.
27 Purnima, V. Sharma, L. Priya, M. Deo, S. Kundu and P. Kar, *Ionics*, 2025, **31**, 1597–1609.
28 A. K. Tripathi, A. K. Ray, S. K. Mishra, S. M. Bishen, H. Mishra and A. Khurana, *Rev. Bras. Farmacogn.*, 2023, **33**, 272–287.
29 R. Lei, W. Wang, G. Li, Q. Yu, H. Fang, J. Xu, K. Zhang and Y. Ye, *J. Nanobiotechnol.*, 2025, **23**, 86.

30 C. Mohanty, A. Samal, A. K. Behera and N. Das, *ACS Omega*, 2024, **9**, 19968–19981.
31 R. W. Peeling and R. McNerney, *Expert Rev. Mol. Diagn.*, 2014, **14**, 525–534.
32 P. Kar, A. K. Behera, B. Adhikari and N. C. Pradhan, *High Perform. Polym.*, 2010, **22**, 428–441.
33 I. Horcas, R. Fernández, J. M. Gómez-Rodríguez, J. Colchero, J. Gómez-Herrero and A. M. Baro, *Rev. Sci. Instrum.*, 2007, **78**, 013705.
34 M. Saeed, Z. Saddique, A. Mujahid and A. Afzal, *Biosens. Bioelectron.*, 2024, **247**, 115899.
35 M. Margoshes and V. A. Fassel, *Spectrochim. Acta*, 1955, **7**, 14–24.
36 O. Abbas, G. Compère, Y. Larondelle, D. Pompeu, H. Rogez and V. Baeten, *Vib. Spectrosc.*, 2017, **92**, 111–118.
37 C. Ö. Dinç, S. Yalçınkaya, H. Altuntaş and N. Çolak, *Des. Monomers Polym.*, 2014, **17**, 629–636.
38 P. Larkin, *Infrared and Raman Spectroscopy: Principles and Spectral Interpretation*, Elsevier, Waltham, MA, USA, 2011.
39 N. C. L. Madeira, P. da, S. Ferreira, J. F. Allochio Filho, L. S. Jr. Chinelatto, M. C. C. Cravo, A. T. Martins, V. Lacerda Jr. and W. Romão, *Energy Fuels*, 2021, **35**, 14553–14568.
40 J. K. Jeon, J. Lee and J.-Y. Imm, *Process Biochem.*, 2014, **49**, 1189–1195.
41 T. Gopalasamy, M. Gopalswamy, M. Gopichand and J. Raj, *J. Polym.*, 2014, **2014**, 827043.
42 A. Rehman, M. A. Ehsan, A. Afzal, A. Ali and N. Iqbal, *Analyst*, 2021, **146**, 3317–3327.
43 A. Lasia, *Electrochemical Impedance Spectroscopy and its Applications*, Springer, New York, NY, 2014.
44 H. Zhang, L. Cheng, H. Shang, W. Zhang and A. Zhang, *Russ. J. Electrochem.*, 2021, **57**, 872–884.
45 E. P. Randviir and C. E. Banks, *Anal. Methods*, 2022, **14**, 4602–4624.
46 A. J. Bard, L. R. Faulkner and H. S. White, *Electrochemical Methods: Fundamentals and Applications*, John Wiley & Sons, Hoboken, NJ, USA, 3rd edn, 2022.
47 C. Liu, Z.-C. Sun, W.-Y. Pei, J. Yang, H.-L. Xu, J.-P. Zhang and J.-F. Ma, *Inorg. Chem.*, 2021, **60**, 12049–12058.
48 K. Maryam, M. U. Javed, C. Rafique, A. Habib and A. Afzal, *J. Electrochem. Sci. Eng.*, 2024, **14**, 787–801.
49 S. Athar, I. Zaman, A. Liaqat and A. Afzal, *ACS Appl. Polym. Mater.*, 2023, **5**, 10438–10445.
50 M. E. Weese-Myers and A. E. Ross, *Electroanalysis*, 2023, **35**, e202200560.
51 T. Abhishek Singh, V. Sharma, N. Thakur, N. Tejwan, A. Sharma and J. Das, *Inorg. Chem. Commun.*, 2023, **150**, 110527.
52 G. J. Brug, A. L. G. van den Eeden, M. Sluyters-Rehbach and J. H. Sluyters, *J. Electroanal. Chem. Interfacial Electrochem.*, 1984, **176**, 275–295.
53 K. Nakano, T. Sato, M. Tazaki and M. Takagi, *Langmuir*, 2000, **16**, 2225–2229.
54 R. Mohanraj, R. Brindha, R. Kandeeban, M. Mahendhar, K. Saminathan and G. Ayyappadasan, *Mater. Lett.*, 2021, **305**, 130796.
55 A. J. Jesu Amalraj and S.-F. Wang, *Mater. Today Chem.*, 2022, **26**, 101154.
56 V. Ruiz, J. Suárez-Guevara and P. Gomez-Romero, *Electrochem. Commun.*, 2012, **24**, 35–38.
57 S. Mahalakshmi and V. Sridevi, *Electrocatalysis*, 2021, **12**, 415–435.
58 M. A. Hefnawy, S. S. Medany, R. M. El-Sherif and S. A. Fadlallah, *ChemistrySelect*, 2022, **7**, e202103735.
59 Z. Saddique, M. Saeed and A. Afzal, *ACS Appl. Nano Mater.*, 2024, **7**, 13472–13480.
60 M. G. Trachioti, A. Ch Lazanas and M. I. Prodromidis, *Microchim. Acta*, 2023, **190**, 251.
61 Y. I. Kuzin, A. I. Khadieva, P. L. Padnya, A. A. Khannanov, M. P. Kutyreva, I. I. Stoikov and G. A. Evtugyn, *Electrochim. Acta*, 2021, **375**, 137985.
62 V. C. Valsalakumar and S. Vasudevan, *Langmuir*, 2023, **39**, 15730–15739.
63 N. Shahzad and A. Afzal, *Microchim. Acta*, 2025, **192**, 163.
64 Y. Li, A. L. Keller, M. T. Cryan and A. E. Ross, *ACS Meas. Sci. Au*, 2022, **2**, 96–105.
65 S. Baluta, F. Meloni, K. Halicka, A. Szyszka, A. Zucca, M. Itria Pilo and J. Cabaj, *RSC Adv.*, 2022, **12**, 25342–25353.
66 D. A. Armbruster and T. Pry, *Clin. Biochem. Rev.*, 2008, **29**, S49–S52.
67 Z. Saddique, M. Saeed, M. Faheem, S. Z. Bajwa, A. Mujahid and A. Afzal, *Nanoscale Adv.*, 2024, **6**, 3644–3654.
68 S. Lu, K. Zhang, Y. Liu, X. Zhan and R. Savari, *Environ. Res.*, 2024, **245**, 117369.
69 O. Corduneanu, M. Garnett and A. M. O. Brett, *Anal. Lett.*, 2007, **40**, 1763–1778.
70 D. M. Stankovic, E. Mehmeti and K. Kalcher, *Anal. Sci.*, 2016, **32**, 847–851.
71 A. P. M. Ferreira, L. N. dos Santos Pereira, I. S. da Silva, S. M. C. N. Tanaka, A. A. Tanaka and L. Angnes, *Electroanalysis*, 2014, **26**, 2138–2144.
72 G. Ziyatdinova, T. Antonova, V. Vorobev, Y. Osin and H. Budnikov, *Monatsh. Chem.*, 2019, **150**, 401–410.
73 G. K. Ziyatdinova, L. V. Grigor'eva and G. K. Budnikov, *J. Anal. Chem.*, 2009, **64**, 185–188.
74 R. Sasikumar, P. Ranganathan, S.-M. Chen and S.-P. Rwei, *Sens. Actuators, B*, 2018, **255**, 217–225.